Wear 321 (2014) 25–32

Contents lists available at ScienceDirect

Wear

journal homepage: www.elsevier.com/locate/wear

Tool wear mechanisms in friction stir welding of Ti–6Al–4V alloy

Jiye Wang [a], Jianqing Su [b], Rajiv S. Mishra [b,*], Ray Xu [c], John A. Baumann [d]

[a] Department of Materials Science and Engineering, Missouri University of Science and Technology, Rolla, MO 65409, USA
[b] Center for Friction Stir Processing, Department of Materials Science and Engineering, University of North Texas, Denton, TX 76203, USA
[c] Rolls-Royce Corporation, Indianapolis, IN 46241, USA
[d] The Boeing Company, St. Louis, MO 63166, USA

ARTICLE INFO

Article history:
Received 21 April 2014
Received in revised form
23 September 2014
Accepted 23 September 2014
Available online 2 October 2014

Keywords:
Friction stir welding
Ti–6Al–4V alloy
Tool wear
WC tools
Lanthanated tungsten tools

ABSTRACT

Friction stir welding (FSW) of titanium alloy Ti–6Al–4V was performed using three types of tools made of W–1.1%La_2O_3 and two different grades of WC–Co based materials. Tool wear characterization was carried out by weight loss measurement, pin profile photographic technique and microscopic observations. Severe tool deformation occurred in the W–La_2O_3 tool with a small conical pin. Deformation was reduced by introducing a larger cylindrical pin design in the W–1.1%La_2O_3 tool. Among the cermet tools, fracture was observed in CY16 grade WC–Co tool with 8 wt% Co but was not found in WC411 grade WC–Co tool with 11 wt% Co. Adhesive wear mechanism was related to the result of chemical affinity between WC–Co and Ti–6Al–4V alloy. Decarburization of WC occurred at tool surface and an interaction layer was observed. Adhesion layer of processed material influenced heat input during FSW and resulted in a narrower heat affected zone (HAZ) in the material processed with the WC–Co tools as compared to the W–1.1%La_2O_3 one. Besides, defects were observed at the bottom of the nugget accompanied by α+transformed β microstructure, which has been discussed in terms of the heat input and strain localization.

© 2014 Elsevier B.V. All rights reserved.

1. Introduction

Titanium alloys are used extensively in the aerospace industry due to their excellent structural efficiency and good high temperature strength [1]. Welding is an effective way to produce a structure with complex geometry and multiple components. Titanium alloys are readily fusion-weldable. However, some problems associated with fusion welding of titanium alloys include porosity, distortion and formation of coarse cast grain structure [2]. Especially for the high strength alloys, fusion welding could produce cast structures with coarse grain sizes resulting in loss of strength in welds and a mismatch of mechanical properties with the base material [1].

The above-mentioned problems associated with conventional fusion welding can be solved by using friction stir welding (FSW). FSW is a promising solid-state joining technique, which has been applied extensively to light alloys like aluminum and magnesium alloys [3]. During FSW, the microstructure experiences dynamic recrystallization due to severe plastic deformation and heat input. Microstructure of titanium alloys can be controlled in FSW through different processing parameters, which leads to retention of the base metal mechanical properties in the weld zone. Pilchak and Williams [4] reported development of equiaxed, bimodal, and lamellar microstructures in FSW of Ti–6Al–4V alloy depending on the peak temperatures reached in the stir zone, which was significantly influenced by the processing parameters.

Although the benefits of FSW are clear, the applications of FSW to alloys with high melting temperature have been limited due to stringent demands on the tool material. First, tools used for high temperature alloys should have excellent mechanical properties at high temperatures to withstand the high load during FSW. Second, tools should have little to no chemical interaction with the material being welded. The tools developed for FSW of titanium alloys include polycrystalline cubic boron nitride (PCBN), tungsten-based refractory alloy, WC–Co material, Mo-based alloy, commercial pure tungsten, TiC and Co-based alloy [2,5–11]. However, limited work has been done on tool evaluations and wear mechanisms.

Ti–6Al–4V alloy is one of the most commonly used titanium alloys. But it is a difficult-to-process material due to its high flow strength at high temperature and low thermal conductivity. FSW of Ti–6Al–4V appeared to be more challenging compared to other titanium alloys. In this work three types of tools, one made of W–1.1%La_2O_3 and two different grades of WC–Co based materials, were used to study the tool performance in terms of tool wear and interactions between the tools and Ti–6Al–4V alloy. Tool wear during FSW could be due to mechanical failure or chemical

* Corresponding author. Tel.: +1 940 565 2316; fax: +1 940 565 4824
E-mail address: Rajiv.Mishra@unt.edu (R.S. Mishra).

http://dx.doi.org/10.1016/j.wear.2014.09.010
0043-1648/© 2014 Elsevier B.V. All rights reserved.

reactions. In the present work, the tool wear mechanism was investigated for the three types of the tool materials. Adhesion of Ti–6Al–4V to WC–Co was observed due to the chemical reaction under compression at 750–1000 °C [12]. The interaction between WC–Co and Ti–6Al–4V and its effect on joint quality and microstructural evolution in FSW were also investigated.

2. Experimental

In this research, bead-on-plate FSW trials were performed on Ti–6Al–4V sheets with a thickness of 2.5 mm. The as-received Ti–6Al–4V alloy had a rolled grain structure consisting of elongated α phase and grain boundary β phase. Tool performance was studied for the three types of tool materials, W–1.1%La_2O_3 and WC–Co based materials of two grades. W–1.1%La_2O_3 rod with a fine-grained worked structure was provided by Midwest Tungsten Services. The two grades of WC–Co based tool materials were provided by Kennametal. One WC–Co material was provided as a sintered rod with the grade of CY16 (nominal composition of 73% WC, 8% Co, 8% TiC and 11% TaC), while the other was in the form of powder with the grade of WC411 (nominal composition of 89% WC and 11% Co). All the nominal compositions are in weight percent. For convenience, the three tool materials will be referred to as W–La, CY16 and WC411 correspondingly. A hybrid tool design [13] is used for the CY16 and WC411 tools, in which the WC–Co face and W–Ni–Fe shank are sinter-bonded together as illustrated in Fig. 1. The design is expected to be more effective in preventing tool failure at the shank part as compared to the integrated WC–Co tool. The W–La tool was directly machined to the configuration and dimensions shown in Fig. 1.

A length of 3 in. was selected for each FSW run using one of the three tool materials. The first six runs included a combination of tool rotation rates of 900 revolutions per minute (rpm), 1000 rpm and 1100 rpm, and traverse speeds of 25 and 50 mm per minute. The FSW machine is displacement controlled and equipped with a load sensing device to measure the real time axial force during processing. Argon gas shielding atmosphere was used to minimize oxidation during FSW processes. Tool wear was characterized using a photographic technique and weight loss measurement. The tool weight was measured using a balance with an accuracy of 0.0001 g. It was noticed that some titanium alloy residuals were still bonded on to the used tools, when the tool weight changes were measured. Change in tool appearance due to tool–workpiece interaction is tracked sequentially and revealed in photographs. To further investigate the tool performance, cross section cuts were made along the tool symmetric axes. The cross-section samples were mounted and polished down to 1 μm surface finish. Tool cross sections were examined using an optical microscope and Hitachi S4700 field-emission gun scanning electron microscope (FESEM). Cross-section samples of FSW Ti–6Al–4V samples were prepared perpendicularly to the processing direction. Samples were mechanically polished to 1 μm surface finish, and etched using Kroll's reagent. The weld quality was examined with the optical microscope. Welded Ti–6Al–4V alloy microstructure and tool debris particles distribution were examined by the Hitachi S4700 FESEM.

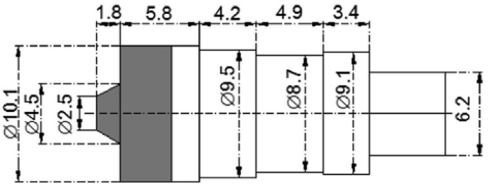

Fig. 1. Configuration of the hybrid tools and dimensions of pin and shoulder. The unit is in millimeter. WC–Co material is shown in the dark shade.

3. Results and discussions

3.1. Tool performance evaluation

Fig. 2 presents the appearance of three tools after different welding lengths. All tools had approximately the same initial configuration and dimensions. Changes in tool configuration were observed in the CY16 and W–La tools after the first trial, while no noticeable change was observed in the WC411 tool after the entire set of six runs. The CY16 and W–La tools experienced different degradation patterns during FSW. The CY16 tool suffered fracture at both pin and shoulder parts without plastic deformation. The pin length was almost constant after FSW. On the other hand such fracture failures were not observed in the W–La tool, which experienced mushroom-type plastic deformation at both pin and shoulder parts. This type of deformation has been also reported in a pure W tool during FSW of L80 steel [14]. Since the CY16 tool experienced severe fracture failure, it was excluded from further tool wear analysis in this study.

The plastic deformation of the W–La tool pin is a function of the FSW stress and temperature and can be reduced by using a large pin. Therefore, a new tool of a cylindrical pin with an increased pin tip diameter of 6.3 mm was used for the additional evaluation and comparison. To distinguish it from the early W–La tool with the small conical pin, the new tool was named as W–La-L, where L denotes "large pin". Appearances of the tools after certain welding lengths are shown in Fig. 3. Although mushroom type of deformation was observed in the W–La-L tool also, it experienced much less plastic deformation as compared to the W–La tool. It should be mentioned that for the W–La-L tool, the first two runs are 3 in. long each under the rotation rate of 1000 rpm and traverse speed of 25 and 50 mm per minute in succession, which is the same as in the first two FSW runs with the W–La tool. For both W–La and W–La-L tools, after the first trial, the tool pin geometry and shape remained almost constant. The tool pin itself undergoes deformation to produce geometries and shape that reduce the net stress. After these trials, an 11 in. long weld run was carried out at 1000 rpm and 25 mm per minute.

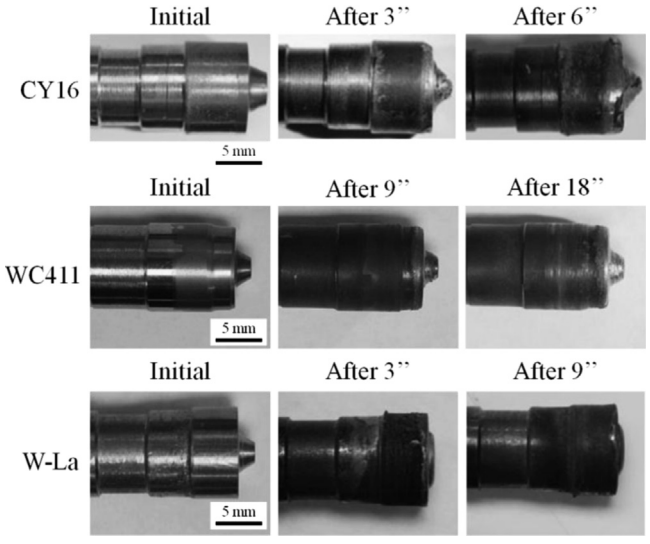

Fig. 2. Appearance of the tools after different welding lengths. Note that the total length of accumulative welds is different for the three different tools.

Fig. 4 shows axial force and estimated stress on pin tip during the first FSW trial using W–La and W–La-L tools. The same processing parameters of 1000 rpm and 25 mm per minute were applied during the first 3 in. FSW trial. Two stress curves were plotted for the W–La tool considering the change of pin size during FSW. The stress at the pin tip was calculated as axial force divided by the pin tip area. The upper limit of stress was calculated based on an initial pin tip diameter of 2.5 mm, and the lower limit was derived from a pin tip size of 5.2 mm measured after welding. As presented in Fig. 4 lower axial force was needed during plunge using the W–La-L tool, which might be due to larger contact area and resultant higher frictional heating. The difference in estimated stresses acting on the pin tips of the two tools was even higher. Stress on the pin of W–La-L tool was around 100 MPa. In comparison, the upper limit of stress on the W–La pin could reach as high as 800 MPa. A transformed β microstructure is observed as discussed later in this paper, which suggests a peak temperature above β-transus temperature (~1000 °C). The ultimate tensile strength (UTS) of W–1.1%La_2O_3 material at 1000 °C was reported to be approximately 500 MPa [15]. The W–La tool with small initial pin size was subjected to the stress above the yield strength, which caused severe plastic deformation at the pin tip.

Fig. 5 shows the weight change versus the weld length for the W–La, W–La-L and WC411 tools. Weight loss was the lowest and almost in a linear relationship to welding length for the WC411 tool. For both W–La and W–La-L tools, weight loss with FSW lengths did not show similar linear relationship. The weight loss of lanthanated tungsten tools was larger as compared to the WC411 tool. Except for the first trial, less weight loss per unit weld length was observed in the W–La-L tool as compared to the W–La tool. For lanthanated tungsten tools, large-sized pin design is preferable to reduce tool wear.

Fig. 6 shows optical microscopy images of cross sections of CY16, W–La and WC411 tools. A crack initiated at shoulder corner, and then penetrated through the pin in CY16 tool. As shown in Fig. 6a, crack bifurcation took place during propagation and resulted in rapid fracture and chipping. Further investigation revealed that shoulder edge and shoulder–pin corner were preferred crack initiation sites, which might be due to stress concentration at these regions. Adhesion occurred between Ti–6Al–4V and CY16 as shown in Fig. 6b. Tool material cracking under the adhesion layer suggests stress concentration caused by pulling force applied by adhered material. Plastic deformation of W–La tool was revealed by the deformed grain structure in Fig. 6c. The formation of stress-induced crack at pin tip could reduce the resistance to wear. No adhesion of Ti–6Al–4V material was observed on W–La tool surface. In the WC411 tool, voids are nucleated at shoulder surface and shoulder corner as shown in Fig. 6e and voids coalescence happens due to localized strain. Such voids were not observed near and at the pin tip. Crack growth was significantly retarded as compared to the CY16 tool. The difference can be attributed to variation of fracture toughness associated

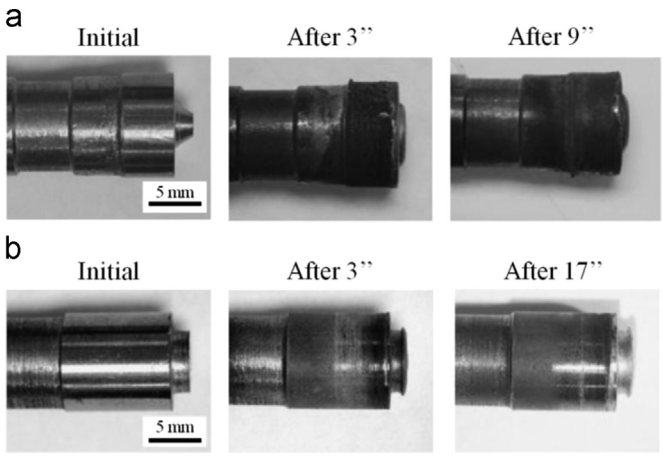

Fig. 3. Changes in tool profiles with increased weld length for (a) W–La tool and (b) W–La-L tool. Note that the total weld length is higher for the W–La-L tool.

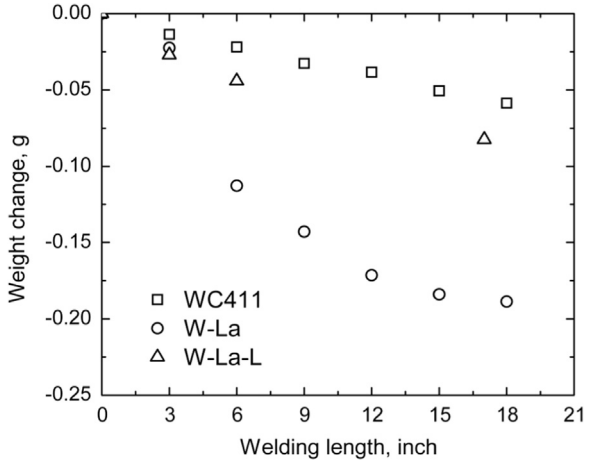

Fig. 5. Weight change versus total welding length for WC411, W–La and W–La-L tools. Note that the weight measurements are done without any physical cleaning of the tool and some Ti–6Al–4V alloy may be sticking to the tool.

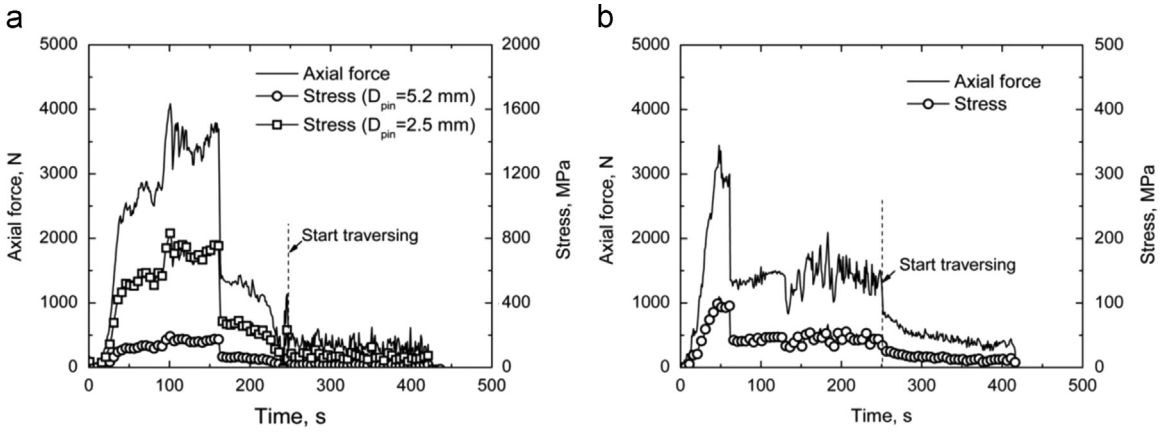

Fig. 4. Axial force outputs and calculated stress acting on pin tip during FSW for (a) W–La tool and (b) W–La-L tool. Two pin diameters (5.2 mm and 2.5 mm) for W–La tool represent, respectively, the initial and final pin diameter.

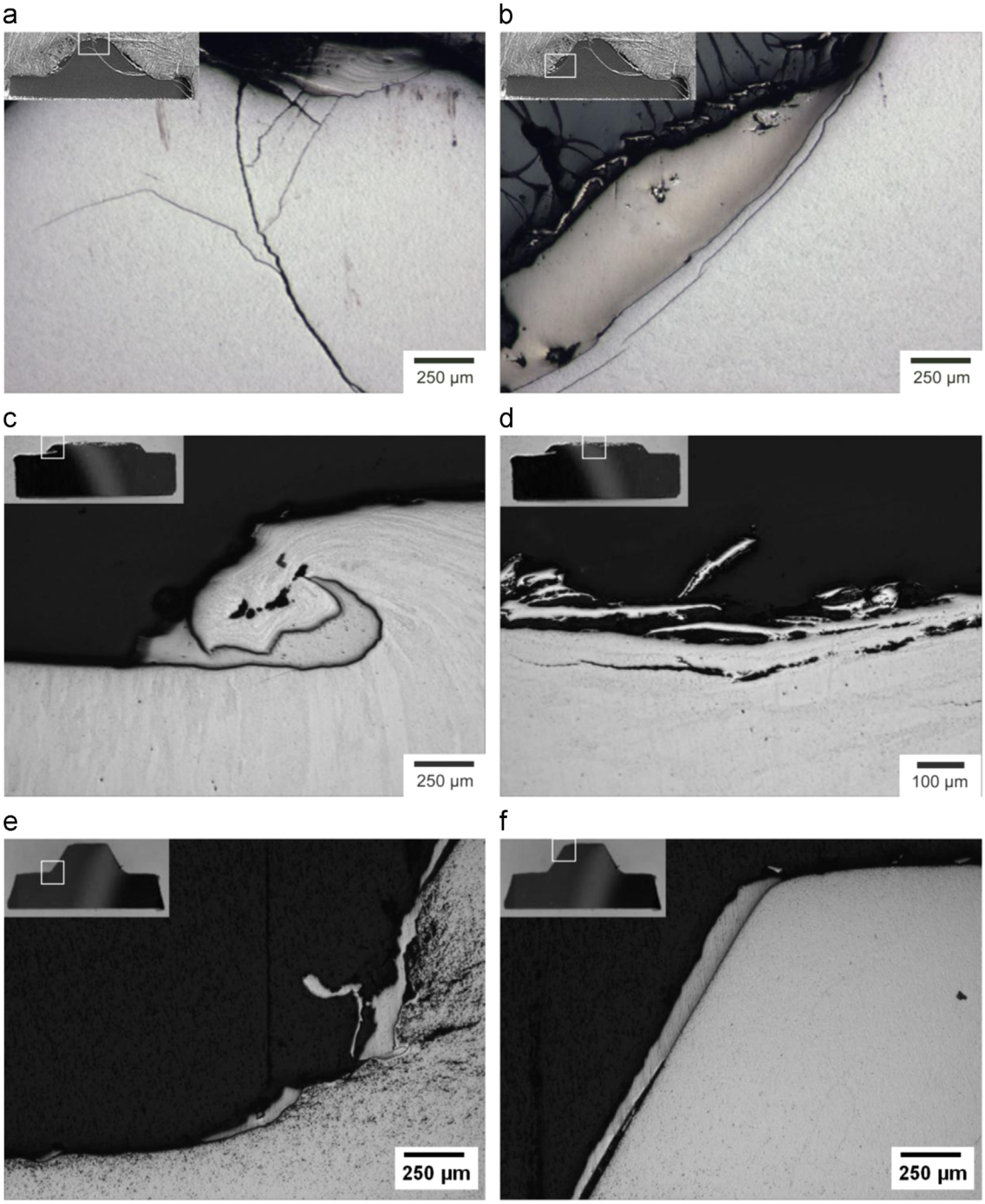

Fig. 6. Optical microscopy images of cross sections of (a, b) CY16, (c, d) W–La, and (e, f) WC411 tools. The inset at left-top corner of each figure. shows a low magnification image and location of higher magnification image.

with chemical composition for tungsten carbides. CY16 has lower cobalt content and less brittle TiC phase, which led to lower fracture toughness compared to WC411. Adhesion layer of Ti–6Al–4V material was also observed on the surface of WC411 tool (Fig. 6f). The observed adhesion of workpiece material is consistent with research carried out by Farias et al. [16]. In their work the EDS mapping results revealed presence of elements of Ti, Al and V, which indicated a strong interaction between the WC tool and Ti–6Al–4V alloy.

To reveal the details of the tool–workpiece interaction, backscattered SEM analysis of the tool cross-section is performed under a magnification of 10,000 × as shown in Fig. 7. The results show the existence of a reaction zone between the workpiece and tool material with a thickness around 100–400 nm. The reaction layer, exhibiting irregular boundary, was composed of many nano-sized grains, and new formed grains extended into adhered Ti–6Al–4V material. The reaction zone could be sheared off and the product material was then transported to the weld zone as shown in Fig. 7b. Formation of a reaction zone at WC interface has been observed and investigated in a WC reinforced Ti–6Al–4V alloy which was produced through the laser melt injection process [17,18]. New phases of W_2C, W and TiC were reported to form in the reaction zone and the following reactions between Ti and WC were proposed,

$$WC + Ti \rightarrow TiC + W \quad (1)$$

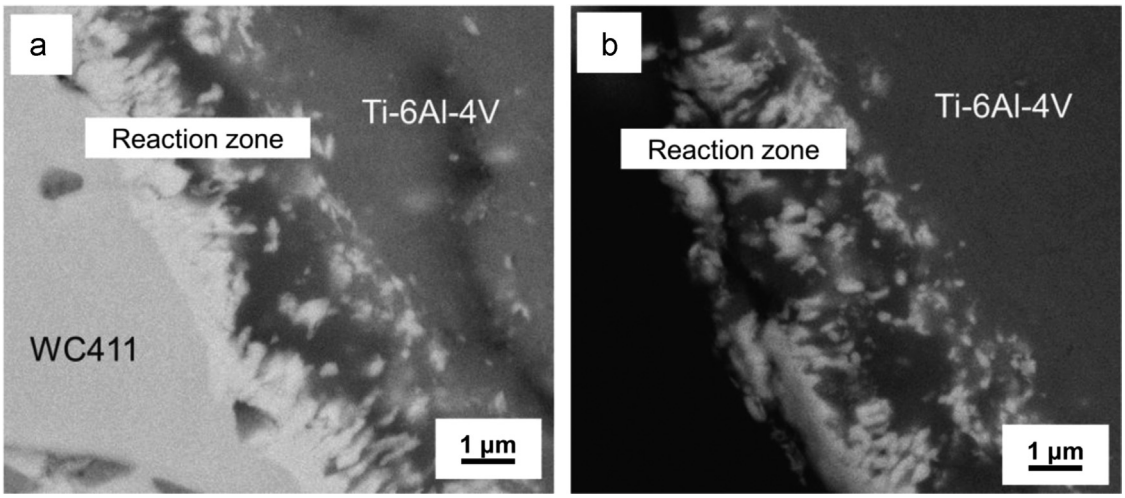

Fig. 7. Backscattered SEM images showing (a) formation of reaction zone at pin surface and (b) the product layer was "sheared off" from WC411 tool.

$$2WC + Ti \rightarrow W_2C + TiC \quad (2)$$

Fig. 8 shows free energy change for reactions (1) and (2) with temperature ranging from 900 K to 1800 K. The free energy was calculated with the data from Binnewies and Milke [19]. The local temperature at reaction zones was assumed to fall in this range during FSW. The resulting negative free energy changes of both reactions suggest that W and W_2C products are thermodynamically possible.

The results cited above indicate that tool performance during FSW is greatly influenced by the tool materials. Tool wear mechanism can be determined either by its chemical reactivity with the processed material and/or by tool mechanical properties. Degradation of W–1.1%La_2O_3 is attributed to plastic deformation due to its low strength at elevated temperature. In this work, a large amount of tool deformation occurred during the first 3 in. length welding trial. After the first trial, tool configuration changed only slightly in the following runs due to reduced stress on the deformed pin part. On the other hand, tool size and weight decreased continuously. Mechanical properties and geometries are both important factors in determining the plastic deformation wear during FSW; the stress-induced cracks were responsible for the majority of tool weight loss.

Chemical reaction between WC–Co tool material and Ti–6Al–4V was attributed to strong affinity between C and Ti at high processing temperatures. The negative free energy change indicated that the decarburization of WC can happen spontaneously at the interface. Further reaction was controlled by carbon diffusion through the reaction layer. As the layer thickness increased, the reaction was retarded. However, the product layer could also be pulled off tool material with adhered Ti–6Al–4V material (Fig. 7b). In this case, a new adhesion layer formed and WC decarburization occurred continuously. The chemical interaction led to the WC–Co tool wear during FSW, and tool wear could also arise due to mechanical interaction. The CY16 tool failure happened by fracture due to its low toughness. With improved fracture toughness, fracture was avoided in the WC411 tool. However, void nucleation and coalescence in WC411 tool have the potential of leaving loosely bonded tool material particles in processed material.

3.2. *Effect of tool material on weld microstructure and quality*

Weld quality of FSW samples fabricated by different processing parameters was evaluated, as described in the Experimental section. Fig. 9 shows welds processed with different tools under

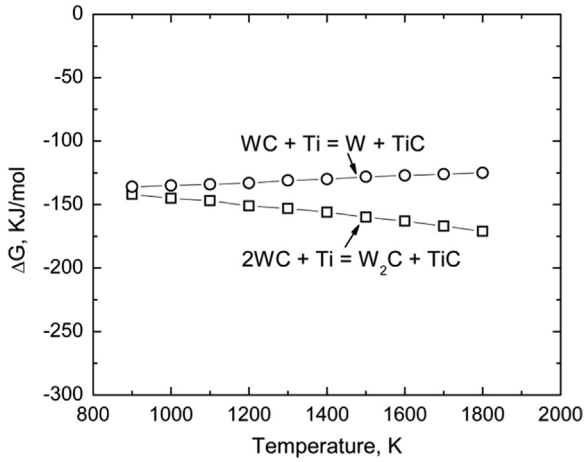

Fig. 8. Calculated Gibbs free energy change for two WC decarburization reactions.

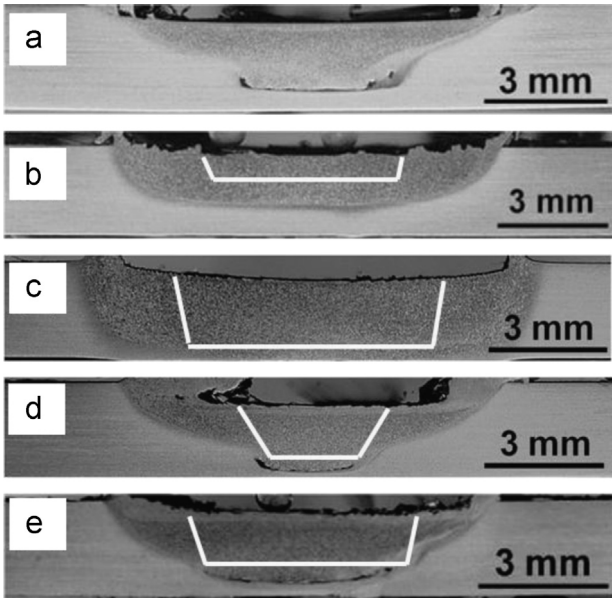

Fig. 9. Optical microscope images of weld cross-sections after FSW with tool rotation rate of 1000 rpm and traverse speed of 50 mm per minute using (a) CY16, (b) W–La, (c) W–La-L, (d) WC411 and (e) WC411-L tools.

the same processing parameters of 1000 rpm rotation rate and 50 mm per minute traverse speed applied in the second 3 in. run for each tool. The total history of welding length at the cross-section location is 5 in. Pin profile outlines have been superimposed on the nugget images except for severely damaged CY16 tool. The welding was performed after the first run; therefore lanthanated tungsten tools experienced only minor changes in profile under the processing parameters since most deformation happened during the first weld with 3 in. length. The WC411 grade WC–Co tool with a large pin was introduced with the pin configuration delineated in Fig. 9(e). The tool has a diameter of 4.5 mm at pin tip, a diameter of 5 mm at pin bottom, and a pin length of 1.7 mm. The tool was termed as WC411-L to distinguish it from aforementioned WC411 tool with geometries shown in Fig. 1. For the same range of applied FSW parameters no defect was observed in FSW samples with W–La and W–La-L tools, while defects were noticed at the bottom of nugget corresponding to pin tip location for each trial with CY16, WC411 and WC411-L tools.

The basin-shaped nugget observed in all the welds (Fig. 9) formed as a result of extreme deformation and frictional heating of the upper surface experienced by contact with shoulder [20]. The nugget width reduced with depth from the top surface. For welds processed with tungsten carbide tools, nugget width was close to the shoulder diameter at the top surface and reduced to pin tip size at the bottom. However, in samples processed with lanthanated tungsten, enlarged nugget zones were observed, especially at the bottom region. The WC411-L tool was introduced to exclude the influence due to different pin sizes. With approximately the same pin size and configuration, nugget volume differed significantly in material processed by W–La-L and WC411-L tools as shown in Fig. 9c and e.

This fact could be attributed to the difference in heat input during FSW with the different tool materials and resultant size of HAZ. During FSW, heat is generated due to friction and plastic deformation, and the contributions to the total heat input are different. The majority of heat was generated by frictional heat. From a computational model for FSW of 7075 Al alloy Bastier et al. [21] report that the overall magnitude of heat generation due to plastic deformation is small, accounting for only 4.4% of the total heat generation whereas frictional heat generation provides 95.6%. In the present study, Ti–6Al–4V adhered to WC–Co tools due to tool–workpiece interaction; i.e., more material "sticks" to the tool. It resulted in an enhancement in shear deformation but reduction in friction interaction between the tool and the processed material. Thus much lower heat was produced, resulting in a smaller nugget volume and insufficient material flow below the pin. This sharper temperature gradient and lack of vertical material flow with WC-based tools led to defects at the bottom of the pin.

Fig. 10 presents backscattered SEM images of microstructural distribution in W–La-L tool processed material, which is the same material shown in Fig. 9c. Fully lamellar structure was developed at all the marked locations. The prior β grain size was around 20–30 μm. The fully transformed β grain structure indicated that the peak temperature in the FSW was above the β-transus temperature. Tool debris particles were observed mainly at top surface and locations in contact with the pin tip. The particle sizes were in a range from submicron to around 3 μm.

Fig. 11 shows backscattered SEM images of microstructure in a WC411 processed sample. In contrast to the W–La-L processed material, the microstructural distribution varied dramatically in the stir zone. Up to 100 μm below the upper surface, fine

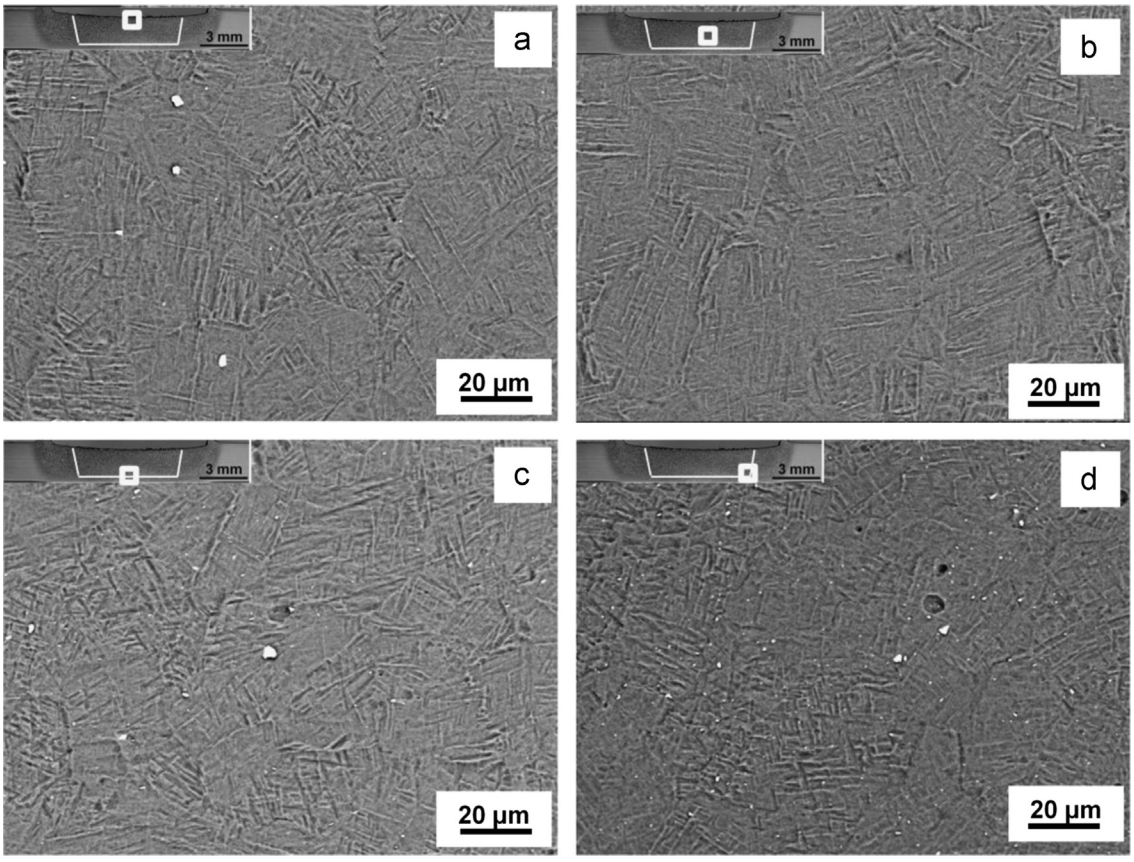

Fig. 10. Backscattered SEM images showing microstructural distribution in W–La-L processed material as a function of location.

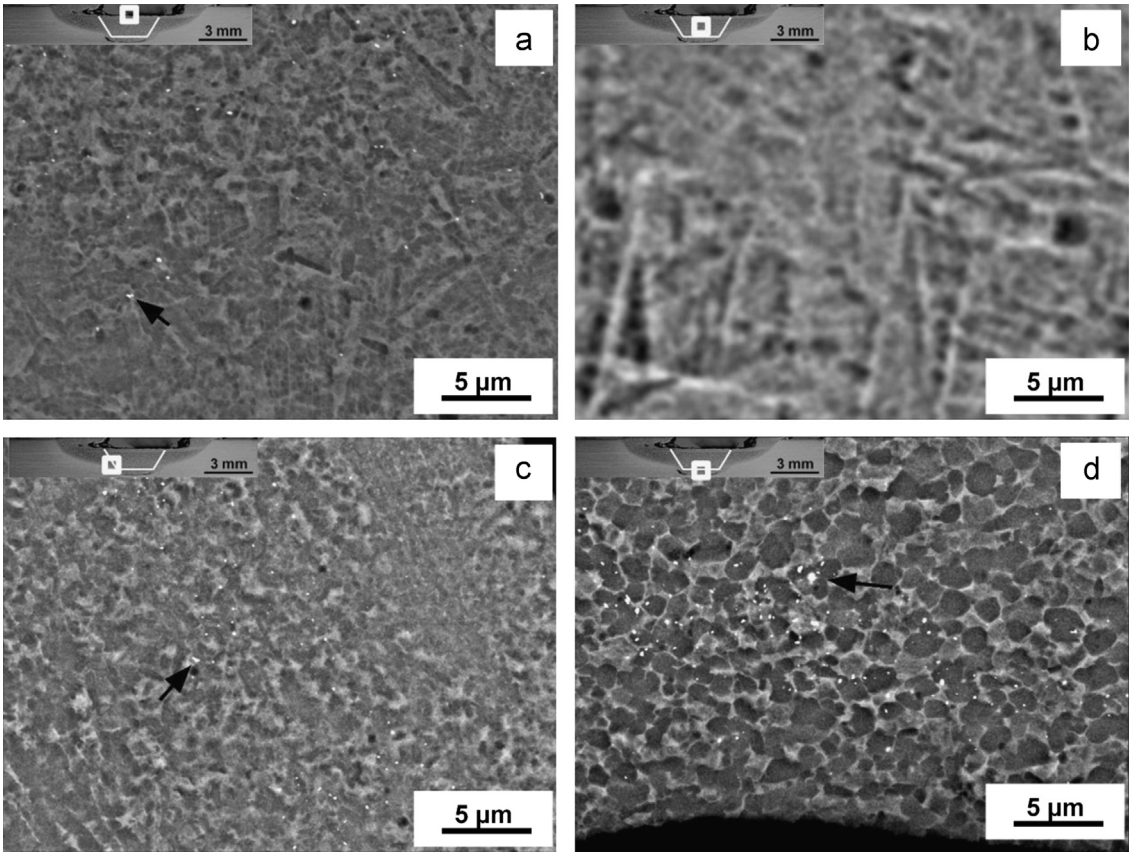

Fig. 11. Backscattered SEM images showing microstructural distribution in WC411 processed material as a function of location (the arrows mark the tool debris).

deformed α and transformed β microstructure was observed. In the center region of nugget, the fully lamellar microstructure as shown in Fig. 11b indicates the peak temperature above β-transus temperature. At the bottom of the nugget, equiaxed α phase and fine transformed β phase were observed. Worth noting is that the defect occurred at the bottom of nugget, where the bimodal microstructure developed. Particle debris was at the regions corresponding to pin profile and tool shoulder. The tool debris particles were in the submicron range. Although void nucleation and coalescence in the WC411 tool can bring about the possibility of leaving loosely bonded tool material particles in processed material Fig. 11 shows the presence of overwhelmingly sub-micron sized tool debris particles, which suggests that tool wear is determined mainly by chemical interaction in the WC411 tool.

Adhesion between the processed material and tool could affect heat input and material flow during FSW, which in turn could influence the final microstructure and weld quality. In WC411 processed material, the presence of deformed α phase and refined transformed β phase near the top surface indicated that very strong shear deformation was experienced by the material sticking to the tool shoulder. In addition, it also proves that the temperature at the periphery of shoulder is below β-transus temperature due to low heat input. The low heat input led to a bimodal microstructure at the bottom of the nugget. The defect formation could be attributed to high strain rate during FSW with strain localization at temperature below β-transus. In the (α+β) phase field, adiabatic heating due to low thermal conductivity resulted in localized flow softening and strain localization by formation of an intense shear band [1]. High strain rate in FSW favored the strain localization. Prasad et al. [22] studied hot deformation of Ti–6Al–4V; the material exhibited a wide regime of flow instability below β-transus. The defects could possibly be eliminated by increasing heat input and decreasing strain rate.

4. Conclusions

The following conclusions can be drawn based on the effects of tool material type on tool wear during the friction stir welding of Ti–6Al–4V alloy:

1. Tool degradation due to plastic deformation was observed in the W–1.1%La_2O_3 tool, and can be reduced by increasing the pin diameter. A self-optimized tool configuration was obtained after the first trial, and little change was observed in the sequent trials. Shear stress-induced cracks were observed at the pin tip and tool debris was left in the processed material. The mechanical fracture along with the diffusion was responsible for tool weight loss.
2. Performance of WC–Co tools was determined by the tool material composition. Fracture failure was observed in the CY16 tool. Microcracking was observed in the WC411 tool with improved fracture toughness, and the crack propagation in the tool was inhibited.
3. Ti–6Al–4V material was bonded to the WC–Co tool surface during FSW. Further investigation showed that a reaction zone formed on the surface of WC–Co tool due to WC decarburization. Existence of adhesion interaction reduced heat input during FSW. Narrow heat affected zone and presence of weld defects were observed. The defects were found in a region with bimodal microstructure of α+transformed β phase, which indicated local processing temperature below β-transus due to low heat input.

Acknowledgment

The authors gratefully acknowledge the Center for Aerospace Manufacturing Technology funding through the CAMT Industrial

Consortium whose active members currently consist of Boeing, Rolls Royce, Spirit AeroSystems, GKN Aerospace, Bell Helicopters, Siemens, KMT Waterjet, and Steelville Manufacturing.

References

[1] G. Lutjering, J.C. Williams, Titanium, Springer-Verlag, New York, NY, 2003.
[2] Y. Zhang, Y.S. Sato, H. Kokawa, S.H.C. Park, S. Hirano, Stir zone microstructure of commercial purity titanium friction stir welded using pcBN tool, Mater. Sci. Eng. A 488 (2008) 25–30.
[3] R.S. Mishra, Z.Y. Ma, Friction stir welding and processing, Mater. Sci. Eng. R: Rep. 50 (2005) 1–78.
[4] A.L. Pilchak, J.C. Williams, Microstructure and texture evolution during friction stir processing of fully lamellar Ti–6Al–4V, Metall. Mater. Trans. A 42 (2011) 773–794.
[5] T.J. Lienert, Microstructures and mechanical properties of friction stir welds in titanium alloys, in: R. Mishra, M. Mahoney (Eds.), Friction Stir Welding and Processing, ASM International, Materials park, OH, USA, 2007, pp. 123–154.
[6] P. Edwards, M. Ramulu, Identification of process parameters for friction stir welding Ti–6Al–4 V, J. Eng. Mater. Technol. (ASME 132 (2010) 0310061–03100610.
[7] J.A. Querin, H.A. Rubisoff, J.A. Schneider, Effect of weld tool geometry on friction stir welded Ti–6Al–4 V, in: S.A. David, T. DebRoy, J.N. DuPont, T. Koseki, H.B. Smartt (Eds.), Proceedings of the Trends in Welding Research, ASM International, Pine Mountain, GA, USA, 2009, pp. pp. 108–112.
[8] Y. Zhang, Y.S. Sato, H. Kokawa, S.H.C. Park, S. Hirano, Microstructural characteristics and mechanical properties of Ti–6Al–4V friction stir welds, Mater. Sci. Eng. A 485 (2008) 448–455.
[9] A.J. Ramirez, M.C. Juhas, Mater. Sci. Forum 426–432 (2003) 2999–3004.
[10] W.B. Lee, C.Y. Lee, W.S. Chang, Y.M. Yeon, S.B. Jung, Microstructural investigation of friction stir welded pure titanium, Mater. Lett. 59 (2005) 3315–3318.
[11] Y.S. Sato, M. Miyake, H. Kokawa, T. Omori, K. Ishida, S. Imano, S.H.C. Park, S. Hirano, Development of a cobalt-based alloy FSW tool for high-softening-temperature materials, in: R. Mishra, M.W. Mahoney, Y. Sato, Y. Hovanski, R. Verma (Eds.), Proceedings of the Friction Stir Welding and Processing VI, TMS, Hoboken, NJ, USA, 2011, pp. pp. 3–9.
[12] C.M. Moreno, G. Artola, J.M. Sanchez, Interaction between Ti–6%Al–4%V alloys and hardmetals coated by cathodic-arc technology, Mater. Sci. Forum 492–493 (2005) 353–358.
[13] J. Rodelas, R.S. Mishra, G. Hilmas, W. Yuan, Mechanical evaluation of friction stir spot welded advanced high strength steels, in: R.S. Mishra, M.W. Mahoney, T.J. Lienert (Eds.), Proceedings of Friction Stir Welding and Processing V, TMS, San Francisco, CA, USA, 2009, pp. pp. 171–179.
[14] W. Gan, Z.T. Li, S. Khurana, Tool mushrooming in friction stir welding of L80 steel, in: R.S. Mishra, M.W. Mahoney, T.J. Lienert, K.V. Jata (Eds.), Proceedings of the Friction Stir Welding and Processing IV, TMS, Orlando, FL, USA, 2007, pp. pp. 279–283.
[15] M. Mabuchi, K. Okamoto, N. Saito, T. Asahina, T. Igarashi, Deformation behavior and strengthening mechanisms at intermediate temperatures in W–La_2O_3, Mater. Sci. Eng. A 237 (1997) 241–249.
[16] A. Farias, G.F. Batalha, E.F. Prados, R. Magnabosco, S. Delijaicov, Tool wear evaluations in friction stir processing of commercial titanium Ti–6Al–4V, Wear 302 (2013) 1327–1333.
[17] J.A. Vreeling, V. Ocelík, J.T.M. De Hosson, Ti–6Al–4V strengthened by laser melt injection of WC_p particles, Acta Mater. 50 (2002) 4913–4924.
[18] L. Li, D. Liu, Y. Chen, C. Wang, F. Li, Electron microscopy study of reaction layers between single-crystal WC particle and Ti–6Al–4V after laser melt injection, Acta Mater. 57 (2009) 3606–3614.
[19] E. Binnewies, E. Milke, Thermochemical Data of Elements and Compounds, 2nd edn, Wiley-VCH, Weinheim, Germany, 2002.
[20] Y.S. Sato, H. Kokawa, M. Enomoto, S. Jogan, Microstructural evolution of 6063 aluminum during friction-stir welding, Metall. Mater. Trans. A 30 (1999) 2429–2437.
[21] A. Bastier, M.H. Maitournam, K. Dang Van, F. Roger, Steady state thermo-mechanical modelling of friction stir welding, Sci. Technol. Weld. Join. 11 (2006) 278–288.
[22] Y.V.R.K. Prasad, T. Seshacharyulu, S.C. Medeiros, W.G. Frazier, Effect of preform microstructure on the hot working mechanisms in ELI grade Ti–6Al–4V: transformed β v. equiaxed ($\alpha+\beta$), Mater. Sci. Technol. 16 (2000) 511–516.